

Hover Performance and Acoustics of a 35% Scale Notional eVTOL Rotor.

Charles E. Tinney*, and John A. Valdez†

Applied Research Laboratories, The University of Texas at Austin, Austin, TX 78713, USA

A first principles understanding of the hover performance and acoustics of a 35% scale notional eVTOL rotor is presented. Measurements are acquired in a large acoustically treated enclosure with rotor speeds corresponding to blade tip Mach numbers and Reynolds numbers around 0.3 and 5×10^5 , respectively. Rotor thrust and torque are measured alongside a line array of microphones traversed between 1.0 and 3.5 rotor diameters from the rotor hub; this captures a two-dimensional map of the pressure field generated by this rotor. Blade collectives are varied from 0 deg to 15 deg in 3 deg increments. Different blade number combinations are studied and comprise a 5-blade, 4-blade, and 3-blade setup. Hover performance measurements at different rotor speeds demonstrate Reynolds number independence with a peak figure of merit of 0.75 at 15 deg collective. Acoustic data are projected to a common distance using spherical decay and a hub centered source. The projection demonstrates that the measurements are, for the most part, being captured in the acoustic regions and that the enclosure and sound treatment are adequate for studying rotors of this scale.

I. Motivation

The rotor scales that most indoor test facilities are appropriately designed for are the ones manufactured for radio control (RC) or small personal drone type vehicles, which are plagued by scaling effects. The most notable of these scaling effects is the Reynolds number associated with the boundary layer that forms over the rotor blade, and the state of the boundary layer, being either laminar, transitional or turbulent. Small, drone-scale rotors have conventional high aspect ratios and comprise small chord lengths (on the order of inches, or fractions thereof) so the boundary layer state is mostly laminar. Next generation tilt-rotors and eVTOL rotors are being designed with less conventional shapes (much lower aspect ratios) and with chord lengths that are still significantly larger than drone scale blades.¹ As such, their boundary layers are either transitioning to turbulence or are fully turbulent at the trailing edge. The state of the boundary layer at the trailing edge is responsible for producing broadband noise, which is a significant noise source of interest to rotor platforms operating in high population density environments where community annoyance can be a concern.²

At present, many of the rotor shapes are designed using both low-fidelity (blade-element momentum theory) and high-fidelity (large-eddy simulation, Reynolds-average Navier Stokes) computational modeling tools.³ These models still rely on quality experimental measurements conducted under known conditions if further refinements to the shape of the blade are to be meaningful. Unfortunately, there are few quality facilities for validating these CFD models under realistic Reynolds numbers and under conditions where both aerodynamic and acoustic factors can be controlled and monitored. That is, the ideal facility must be large enough to prevent rotor recirculation effects from corrupting rotor load measurements, while having sufficient sound treatment for quality acoustic measurements. For example, large indoor whirl towers may be large enough to keep recirculation effects to a minimum, but are often not acoustically treated, while outdoor testing is subject to unpredictable cross winds, temperature gradients and ground reflections. Most academic anechoic chambers provide sufficient sound treatment, but are too small to test rotors larger than the ones found on drone scale systems. Many of the next generation vehicle concepts now comprise multiple smaller

*Senior Scientist; ✉ charles.tinney@arlut.utexas.edu, 🌐 <https://wwwext.arlut.utexas.edu/gdl>. Associate Fellow AIAA

†Engineering Scientist Associate; ✉ john.valdez@arlut.utexas.edu, AIAA Member

rotors, instead of one large conventional rotor, as is seen on the Bell/Boeing V-22 Osprey, Bell V-280 Valor, Leonardo AW609, as well as concepts being proposed for electrical vertical takeoff and landing (eVTOL) by Joby Aviation, Archer Aviation and Vertical Aerospace, to name a few.

The focus of this study is to present new measurements of the aerodynamic and acoustic performance of a notional eVTOL rotor in hover to be offered to the scientific community as a benchmark for model validation. The emphasis of our discussion is on describing the test setup, sources of experimental error, and efforts to gauge the effects imposed by the enclosure in which the measurements are acquired. An overview of this paper is as follows. A description of the facility and hardware is first provided and includes methods for minimizing uncertainties in the test apparatus. Hover performance measurements are then shown for the notional eVTOL rotor operating at two rotor speeds to gauge the significance of Reynolds number effects at this scale. Measurements of the sound field are then presented and are scrutinized for recirculation effects as well as acoustic reflections from the enclosure. The latter is confined mostly to attempts to collapse the acoustic measurements using spherical decay laws and a hub centered source.

II. Facility and Test Apparatus

The rotor blade that has been built for this study is a geometrically scaled replica of the one used on an earlier generation Joby Aviation prototype vehicle flown in 2017 and described recently by Stoll and Bevirt.⁴ This rotor comprises five blades with a full-scale diameter of 2.9 m, an axial thrust of 4 kN at 800/60 rev/s, and a rotor figure of merit of 0.75. Blade chord and twist distributions are shown in Fig. 1a. A 35% geometrically scaled replica of the rotor was then fabricated from 6061 aluminum using computer numeric controlled machining (CNC) resulting in a diameter of $D = 39.96$ in. (0.665 m) and a max chord of $c_{max} = 3.2976$ in. (83.76 mm) at $r/R = 0.40$ ($R = D/2$ is the rotor radius). These stiff aluminum blades reduce blade deflections to negligible levels, but at the expense of increased rotational mass, and a reduction in the maximum allowable rotor speed. The root is rigid without lead-lag and flap hinges, while there is no pre-coning of the blade. At the root ($r/R = 0.15$), the blade twist is $\beta_0 = 26.15$ deg while it measures -9.79 deg at $r/R = 1.0$. The pitch angle reference is determined by setting the blade pitch to zero at $r = 0.75R$; the chord length at this location is valued at $c_{75} = 2.9583$ in. (75.14 mm). Profiles of the blade cross section are shown in Fig. 2a at three radial positions corresponding to $r/R = 0.50$, 0.75 and 0.90. The locations of these profiles are identified in the computer aided design drawing in Fig. 2b. The rotor assembly is designed to accommodate different blade number combinations ranging from five blades (as seen on many of the prototype eVTOL vehicles), down to two blades, as it relates to conventional vehicles. This is intended to provide an opportunity for the trade-space between hover performance and acoustics to be studied for different blade loading conditions.

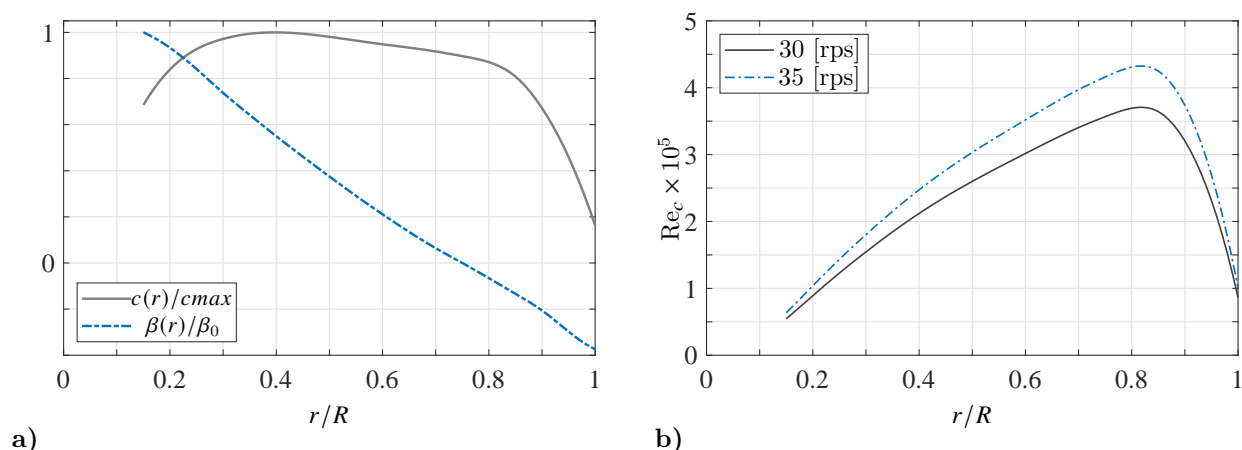


Figure 1: a) Blade chord and twist distribution. b) Reynolds number distribution across the blade.

A new rotor test stand was built for this study and was specifically designed to accommodate larger scale rotors (upwards 40 in. in diameter) such as the one tested here. An image of the new upper assembly during testing is shown in Fig. 4b. Rotors are spun using a 15 kW (maximum) Hacker A200-6 brushless direct-current

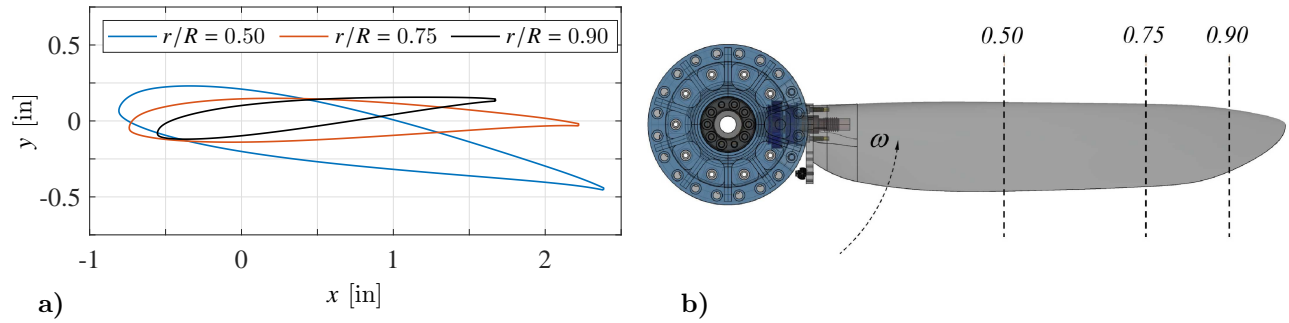


Figure 2: a) Cross sections of the notional eVTOL rotor blade at three radial locations and b) computer aided design drawing of the blade with hub and pitch horn.

motor (BLDC) that is housed within an aluminum shell in order to reduce motor noise from contaminating sound measurements of the rotor. Motor power is provided by a battery bank consisting of two Zee 6S LiPo Batteries with a capacity of 10000 mAh, a voltage of 22.2 V, and 120 C output rating connected in series resulting in a 12-S battery bank of 44.4 V. Power and rotation speed are governed using a VESC 75-300 electronic speed controller (ESC) capable of delivering a maximum continuous current of 300 Amp. Motor speed is then monitored and controlled using a combination of the “VESC Tool” with National Instruments LabVIEW; the software/hardware combination was specifically chosen to improve motor performance while reducing thermal losses and overheating. Feedback to the speed controller is provided by way of a AMS AS5147U magnetic rotary encoder mounted to the base of the motor and with a bipolar magnet attached to the motor shaft. Quadrature encoder outputs are recorded using a National Instruments compactRIO system. The hardware/software combination allows for angular resolutions of $360\text{deg}/(4 \cdot 1024) \sim 0.0879$ deg over the full duration of testing. Rotor pitch is controlled using a servo actuated swash-plate using three hi-torque servos acting in unison as shown in Fig. 3a. The swash-plate allows collective pitch control only and is designed to accommodate a 20 deg range of rotor pitch angles without having to adjust pitch links. Pitch link threads, combined with the pitch horn, provide an angular resolution of 0.35 deg per half turn. Blade pitch angles are measured using a 0.1 deg accurate digital angle indicator. The digital indicator is mounted to a 3D-printed sleeve that fits snug around the blade tip in order to improve the accuracy and repeatability of the readings. An image of the sleeve with digital indicator is shown in Fig. 3b. Prior to testing, the base of the rotor test stand was shimmed so that the rotor shaft was aligned with the gravity vector (to within the accuracy of the digital indicator).

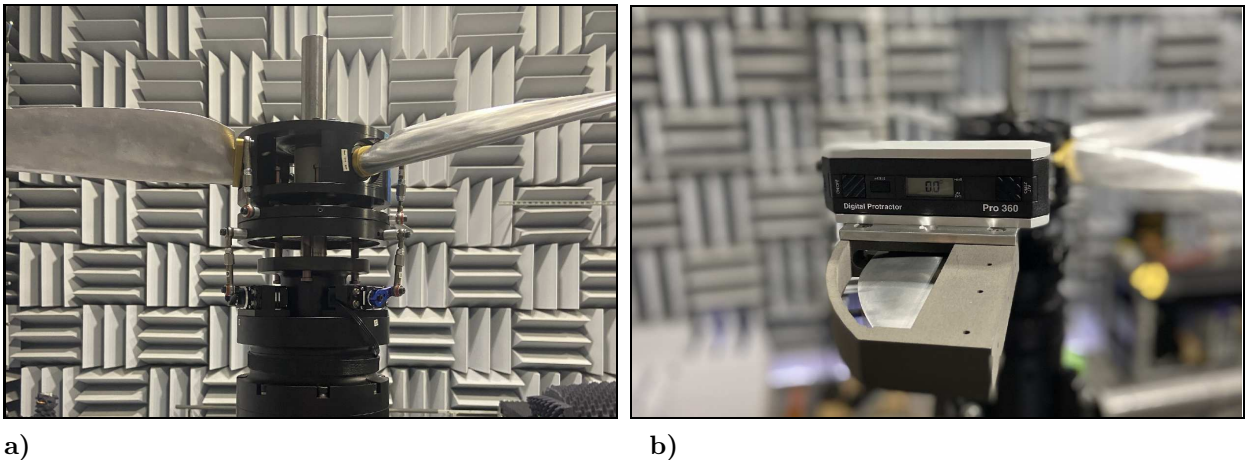


Figure 3: Image of the a) rotor assembly, and b) digital angle indicator with sleeve.

Both the hover performance and acoustic measurements were acquired in the Gas Dynamics Laboratory of the Applied Research Laboratories, The University of Texas at Austin (ARL-UT). The facility is fully enclosed and comprises $V = 30,100 \text{ ft}^3$ of open air space over $1,500 \text{ ft}^2$ of floor space with an average ceiling height of 21 ft; a plan view of the floor space is shown in Fig. 4a. The majority of surfaces are treated with

acoustic panels with a normal incidence sound absorption coefficient of 99% above 100 Hz. The facility is located in Austin, Texas near sea-level conditions where $p_\infty = 14.7$ psia (103,325 Pa), $T_\infty = 529$ R (294 K), $\gamma = 1.4$, and $\rho = 2.33 \times 10^{-3}$ slug/ft³. This equates to a sound speed of $c_o = 1128$ ft/s for the surrounding air. This same facility and acoustic treatment has been used successfully to study the hover performance and acoustics of various drone scale systems.⁵⁻⁷ However, past studies were confined to diameters no larger than 18 in.

Facility planview

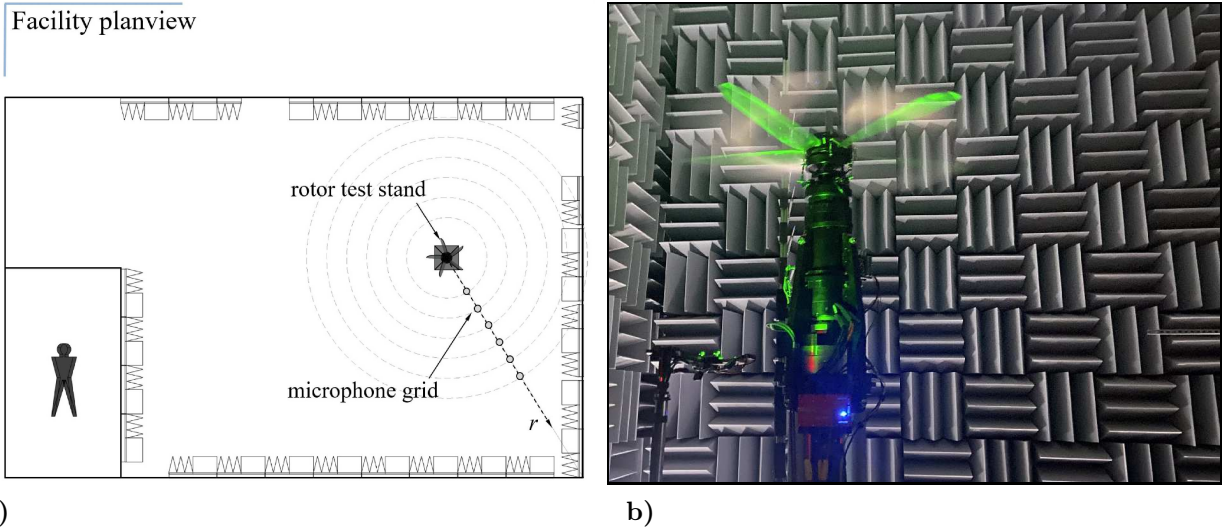


Figure 4: a) Plan view of the Gas Dynamics Laboratory at The University of Texas at Austin with rotor setup and microphone array. b) Image of the rotor spinning during preliminary testing.

The matrix of test conditions to be filled in with this new setup is provided in Table 1. The conditions marked by filled symbols (● and ●) have been completed, while conditions marked by empty symbols ○ will be performed subsequent to this article. Furthermore, markers color coded by ● identify databases described in this article.

Table 1: Matrix of available databases of the acoustics and performance of the notional eVTOL rotor in hover for all pitch angles ($\alpha = 0, 3, 6, 9, 12, 15$ deg) and the full microphone grid.

N_b	Performance			Acoustics		
	30 [rps]	35 [rps]	40 [rps]	30 [rps]	35 [rps]	40 [rps]
5	●	●		●		
4	●	●		●		
3	○	○		●	●	●
2	○	○		●		

III. Hover Performance

Thrust and torque were measured using a Interface Model 1216 bi-axial load cell with a 1000-lbf axial force range and a 500 lbf-in. torque range. Both non-linearity and hysteresis errors, as reported by the manufacturer, are 0.04% and 0.07% of full-scale output for the axial and torsion bridges. This equates to errors of ± 0.4 lbf and ± 0.35 lbf-in. in thrust and torque measurements, respectively. Load cell readings were recorded at 20 kHz for a duration of 32.77 seconds after the rotor had spun up to steady state conditions and the wake had settled. The high sampling speed was chosen in order to monitor the rotor assembly for lateral motions that would result in bending moments on the load cell and ultimately corrupt its readings. Hover performance measurements reported here are evaluated for the 5-bladed rotor and for two rotor speeds

corresponding to $\omega = 30$ rps (rotations per second) and $\omega = 35$ rps (the findings using other blade number combinations and rotor speeds will be reported elsewhere). The Reynolds number distribution across the blade for these two rotor speeds is shown in Fig. 1b and is calculated without inflow corrections. Peak Reynolds numbers for these speeds are valued at 3.71×10^5 , and 4.32×10^5 , respectively, and are found at $r/R = 0.82$ where the chord is 2.8126 in. (71.44 mm). The corresponding blade tip Mach numbers are 0.278, and 0.325, respectively.

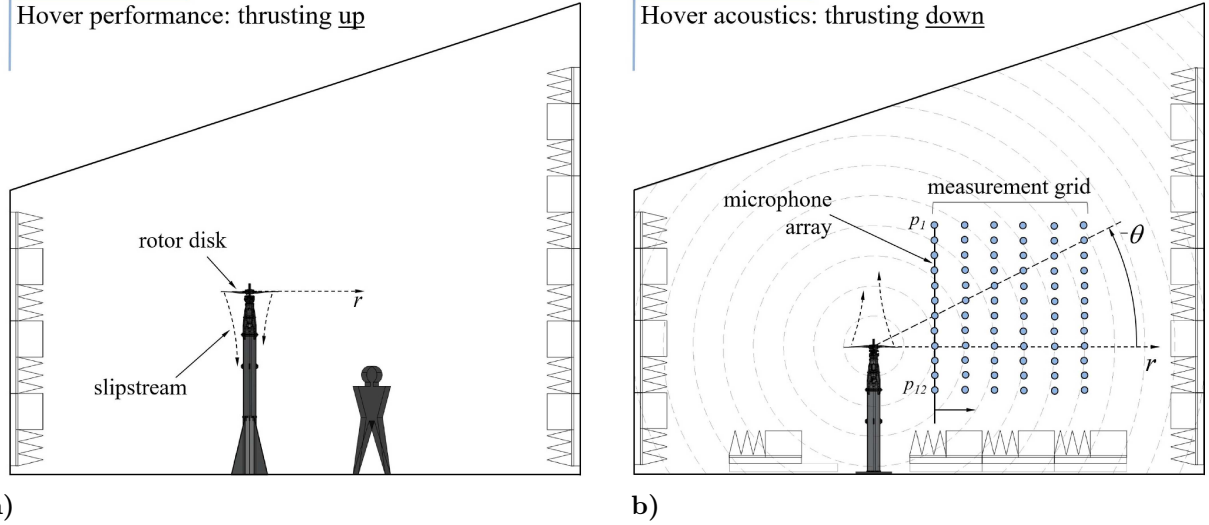


Figure 5: Rotor setup sideview for a) hover performance (thrusting up) and b) acoustics (thrusting down) in the GDL.

For these measurements, the rotor disk plane was elevated 120 inches from the laboratory floor and with the thrust vector pointing up, as shown in Fig. 5a. This height is considered sufficient for reducing ground effects,^{10–12} though it was found that the insertion of nearby acoustic floor panels had no noticeable effect on the measured performance. Average thrust and torque values generated by the 5-bladed rotor are reported in Table 2 and then plotted in Fig. 6a using imperial units; the conversion to the SI system of units is 4.44822 N/lbf and 0.11298 Nm/lbf-in. The corrected average blade pitch is shown in Fig. 6b and identified by α' in Table 2. Values in SI units corresponding to the $\omega = 30$ rps condition are inserted to the right and top of Fig. 6a for the thrust (N) and torque (Nm), respectively. All numbers have been rounded to integer values to reduce clutter while the same symbol and color combinations are used throughout. For the 30 rps condition, the blade pitch was varied up to $\alpha = 18$ deg, while the 35 rps case was only capable of a maximum pitch angle of $\alpha = 15$ deg (for the five blade configuration) due to the current limits of the ESC.

Table 2: Hover performance of the notional 5-bladed eVTOL rotor in hover at (left) 30 rps, and (right) 35 rps rotor speeds.

α [deg]	α' [deg]	$\Delta\alpha'$ [deg]	F_T [lbf]	τ [lbf-in.]	t_v [s]	F_T [lbf]	τ [lbf-in.]	t_v [s]
0	-0.51	0.6	4.32	20.54	335	5.64	27.80	293
3	2.61	—	9.77	24.15	223	12.93	32.18	194
6	5.67	—	15.29	32.99	178	19.96	43.14	156
9	8.68	0.7	21.92	47.80	148	29.42	63.68	128
12	11.65	—	28.88	67.26	130	39.03	89.90	111
15	14.56	0.7	36.41	92.34	115	49.72	124.65	99
18	17.42	—	45.14	127.45	104	—	—	—

Rotor power is shown in Fig. 7a where $P = \tau\Omega$ and $\Omega = 2\pi\omega$ is the motor rotation speed in rad/s. Thrust coefficient (C_T), power coefficient (C_P) and rotor figure of merit (FM) were then computed using the

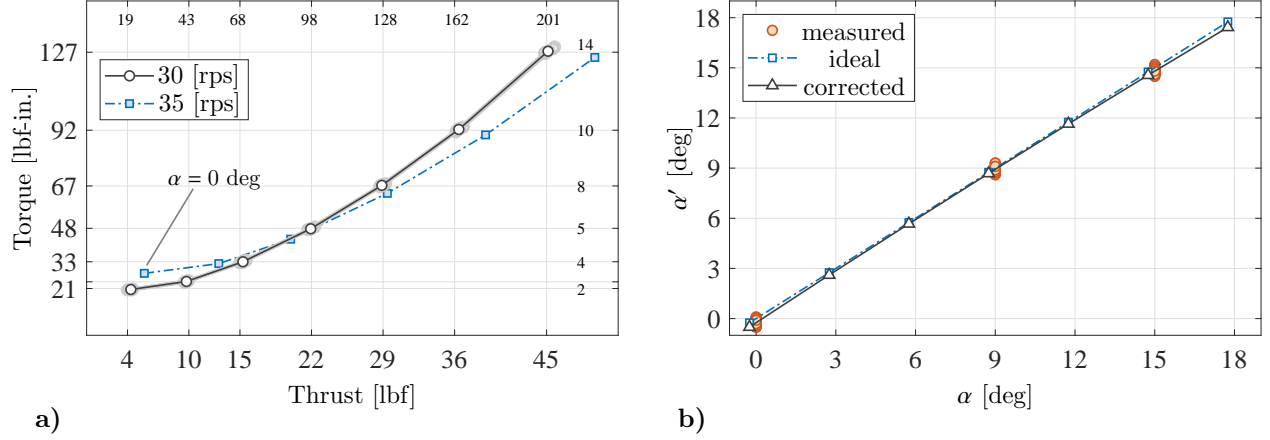


Figure 6: a) Thrust (F_T) and torque (τ) of the 5-bladed rotor in hover for two rotor speeds ($\omega = 30$ rps, and 35 rps). b) Measured and corrected blade pitch angles.

following well known definitions,^{8,9}

$$C_T = \frac{F_z}{\rho A (\Omega R)^2} \quad (1)$$

$$C_P = \frac{\tau \Omega}{\rho A (\Omega R)^3} \quad (2)$$

$$FM = \frac{C_T^{3/2} / \sqrt{2}}{C_P} \quad (3)$$

where $A = \pi D^2/4$ is the disk area. Blade loading coefficients are reported in Fig. 7b where rotor solidity σ is calculated using both the blade area and hub, and is valued at 0.2033 (the hub radius is valued at 3.00 in. (76.2 mm)). Blade area is computed by integrating the chord distribution along the trailing edge and by neglecting small changes along the leading edge.

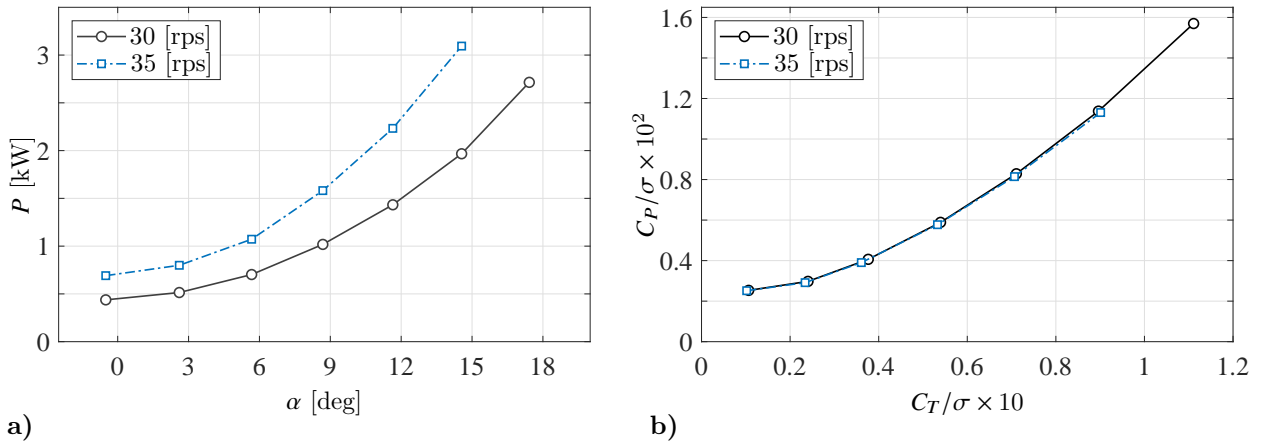


Figure 7: a) Rotor power and b) blade loading coefficient of the 5-bladed rotor in hover for two rotor speeds ($\omega = 30$ rps and 35 rps).

Thrust and power coefficient are shown in Fig. 8a alongside rotor figure of merit in Fig. 8b. Negligible changes on account of increased rotor speeds for a given blade pitch suggests that the performance of this rotor is unaffected by Reynolds numbers at this scale. The peak rotor figure of merit is valued at 0.75 and

is found to occur at $\alpha = 15$ deg. A final calculation involves the facility time scale and is a ratio of the open air volume of the GDL facility to the volume flow rate generated by the rotor,

$$t_v = V / A v_i \quad (4)$$

where $\lambda_i = \sqrt{C_T/2}$ and $v_i = \lambda_i(\Omega R)$ is the rotor inflow. The facility time-scale is a measure of the time required for the rotor to move the full volume of air in the facility. Estimates are listed in Table 2 with the lowest reported value being 99 seconds for the $\alpha = 15$ deg and $\omega = 35$ rps rotor conditions. Other closed-chamber facilities can be shown to have operated on both larger and smaller time scales. For example, based on the conditions reported by McCoy et al.,¹³ the facility time-scale of their setup is estimated to be 74 s (40 in. rotor spinning at 42 rps inside a closed-chamber volume of 41,700 ft³ with an induced velocity ratio of 0.1467). Schiller et al.,¹⁴ based on experiments performed in the SALT anechoic facility at NASA-LRC, reports a two rotor setup in side-by-side configuration (two 12.5 in. diameter blades at 85 rps in a 11,856 ft³ enclosure) which equates to a facility time scale of 232 s (C_T is estimated to be 9.5×10^{-3} for this calculation). At last, the side-by-side rotor configuration recently reported by Pandey et al.¹⁵ in the GDL (two 18 in. diameter blades at 90 rps) is found to be 283 s.

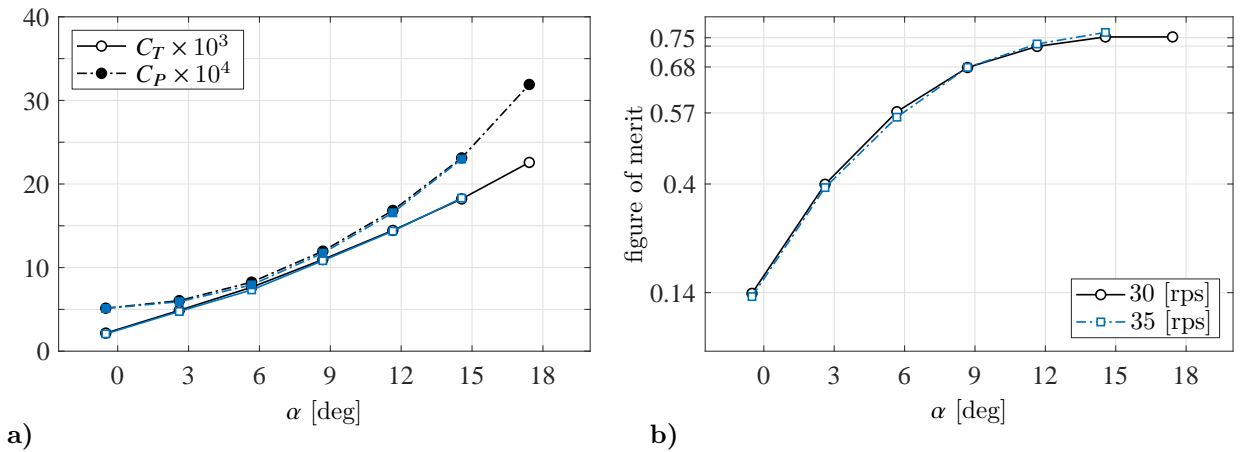


Figure 8: a) Thrust coefficient, power coefficient, and b) rotor figure of merit for the 5-bladed rotor in hover.

IV. Near-Field Acoustics

For these measurements, the base of the rotor test stand was removed thereby placing the rotor disk plane 84.5 in. (2.1 rotor diameters) from the laboratory floor as shown in Fig. 5b. Rotor blades were then inverted so that the thrust vector was pointing down and in the direction of the gravity vector. This new setup has the benefit of increasing the distance between the rotor disk plane and the virtual floor (facility ceiling) to 156 in. (3.9 rotor diameters); recirculating air currents generated by the hover performance setup were corrupting the pressure waveforms captured by the microphones located below the rotor disk and close to the acoustic panels near the floor. A combination of eight G.R.A.S. IEPE-type half-inch free-field microphones (model 46AE with matching model 26CA preamplifiers) and four quarter-inch free-field microphones (model 40BD with matching model 26CB preamplifiers) were used to capture the sound field generated by the rotors. These twelve IEPE type transducers were powered using a National Instruments PXI system (two NI-PXI-4472 boards) with each channel comprising its own 24-bit analog to digital converter and low-pass filter (low pass Butterworth set to 84% of the nyquist frequency). Microphones were arranged to form a line parallel to the rotor axis with the forth sensor (measured from the facility floor) being located at the rotor disk plane and subsequent sensors having equal spacings of $\delta z = 10$ in. The locations of these sensors are shown in Fig. 5b. The microphone array was traversed radially from the rotor hub between $r_1 = 40$ in. ($r/D = 1.0$) to $r_6 = 140$ in. ($r/D = 3.5$) in increments of $\delta r = 20$ in. to form the 2D measurement grid shown in Figs. 4b and 5b. At each of these six stations, microphone signals were digitized at a rate of 50 kHz for an uninterrupted duration of 20.48 s and with microphone caps removed. Digitized signals were converted to engineering units and stored for post-processing. Sound pressure spectrum levels (SPSL, re: $20\mu\text{Pa}$) were

computed using a Hanning window and by ensemble averaging data blocks of $N = 3 \times 2^{13}$ data points per block with 75% overlap. This resulted in a spectral resolution of $f_s/N = \delta f = 2.0345$ Hz. No corrections for atmospheric absorption or human ear effects are accounted for in these spectra. Corrections for diffraction effects for different angles of incidence ($\Delta\Theta_c(f)$ dB) as well as the unique frequency response characteristics of each microphone ($\Delta F_c(f)$ dB, as provided by the manufacturer during calibration) are implemented when calculating these spectra,¹⁶ where $\text{SPSL}_0(f) = \text{SPSL}(f) + \Delta F_c(f) + \Delta\Theta_c(f)$. These corrections only affect the high frequencies, predominantly the ones above 10 kHz.

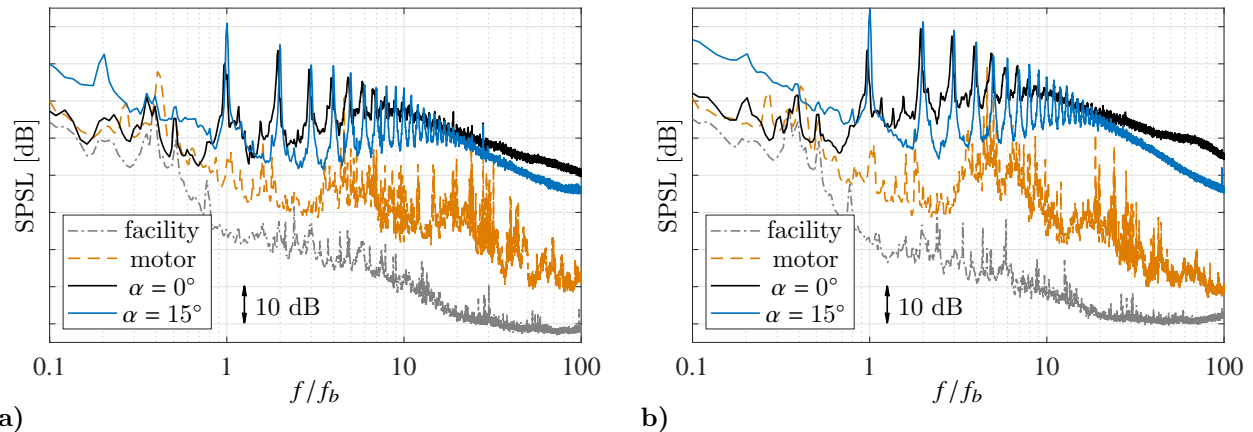


Figure 9: a) Sound pressure spectrum level [dB, re: $20\mu\text{Pa}$] of the facility background noise, motor noise and rotor noise at 30 rps for two pitch angles of the 5-bladed rotor as seen by an observer at $r/D = 2.0$ and the rotor disk plane ($\theta = 0$ deg), and b) below ($\theta = -45$ deg).

A comparison of background facility noise, motor noise, as well as rotor noise measurements at two blade pitch angles (0 deg and 15 deg) is shown in Figs. 9a and 9b for two observer locations at $\theta = 0$ deg and -45 deg, respectively. This is for the 5-bladed rotor. The overall noise generated by this notional eVTOL rotor is much larger than the background noise and motor noise. A pronounced high frequency hump suggests the presence of rotor broadband noise and is affected by the blade pitch angle. Likewise, a change to the pitch angle from 0 deg to 15 deg is shown to reduce the rotor broadband noise levels and is attributed to the ingestion of clean flow into the rotor disk at higher pitch angles.

In order to see if recirculation effects are present and to what degree they may be affecting the acoustics, several tests were performed by measuring both the aerodynamic loads and rotor acoustics during startup to steady state conditions. If the enclosure is too small relative to the scale of the rotor, then one would expect an increase in the higher-harmonic tones to ensue shortly after the rotor reaches its desired rotor speed.¹⁷ Such tones are associated with the unsteady wake becoming re-ingested into the rotor. For this test, the angle of attack of all blades was first set to $\alpha = 15$ deg prior to startup; this is the condition in which the rotor figure of merit was shown to be maximum. The rotor was then spun up to a rotor speed of $\omega = 30$ rps, at which point the rotor speed controller was activated. Two tests are evaluated here for the microphone located along the rotor disk plane. The first corresponds to a gradual 30-second duration startup, and is shown in Fig. 10a, while the second is for a rapid 5-second startup and is shown in Fig. 11.

Starting with Fig. 10a, a spectrogram of the slow startup is shown and is computed over the full 65-second duration of the test (startup and steady state). Ensemble averaged spectra (SPSL) are generated for two 15-second windows shown in Fig. 10a (thirty non-overlapping blocks of data). These spectra are shown superposed one another in Fig. 10b and were generated using the same processing methods described earlier. The overlap in the peak spectral harmonics suggests that the facility and rotor size combination are not corrupted by recirculation effects. A second test is then performed for a rapid 5-second duration startup, and is shown in Fig. 11a. This kind of startup generates impulse changes to the air currents in the facility; a sufficient amount of time between testing allowed existing air currents to settle prior to this rapid startup. Two 5-second windows are also evaluated here in order to isolate the sound field immediately following startup at $t = 5$ s, and then one several minutes later after the wake and air currents in the enclosure have relaxed. One can see how the faster startup takes a few seconds for the rotor to stabilize, as demonstrated by the thrust and torque measurements shown in Fig. 11c,d. The rotor is much quieter during the first window

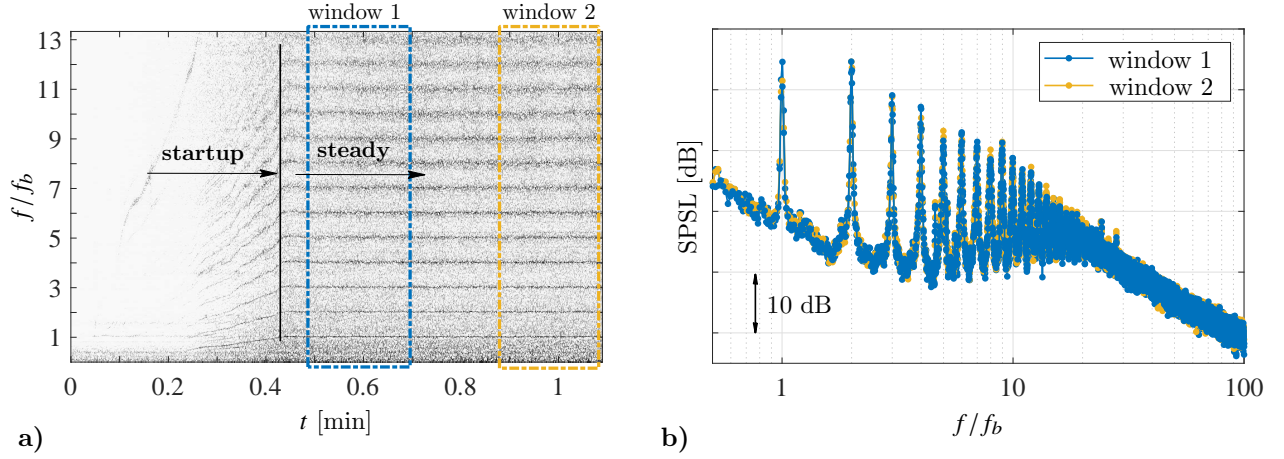


Figure 10: a) Spectrogram of the $\theta = 0$ deg observer at $r/D = 2.0$ during gradual startup of the 5-bladed rotor. b) SPSL for the two 15-second windows shown in (a).

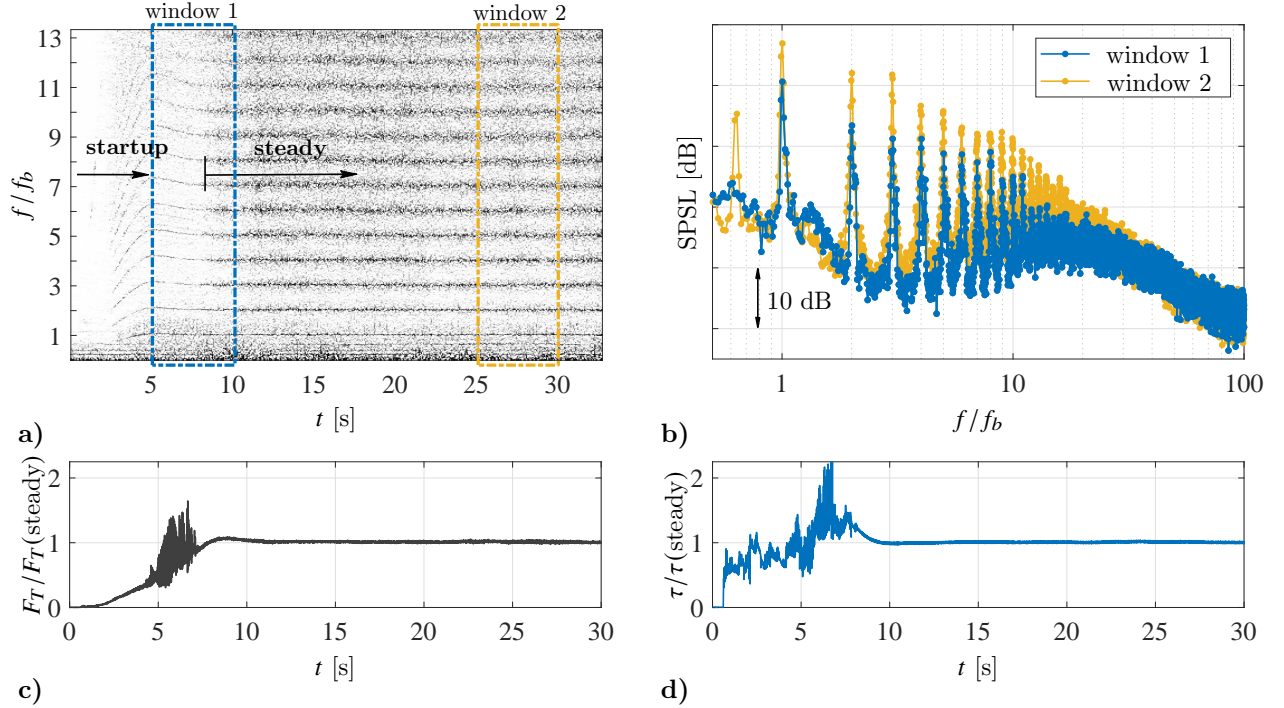


Figure 11: a) Spectrogram of the $\theta = 0$ deg observer at $r/D = 2.0$ during rapid startup of the 5-bladed rotor. b) SPSL for the two 5-second windows shown in (a). c) Rotor thrust and d) torque measured during rapid startup.

in time, compared to the second window starting at $t = 25$ s. Some might attribute these elevated noise levels to facility induced recirculation effects resulting in large-scale turbulence ingestion noise.¹⁸ Conversely, the lower than ambient static pressure in the rotor wake causes air to be entrained through the slipstream. Once the rotor wake has had time to develop, recirculating air currents setup close to the rotor wake, which are inherently unsteady. It is conjectured that in open jet wind tunnels, the wake and slipstream generated by rotors/propellers are not allowed to develop properly, which inhibits the formation of naturally occurring recirculating air currents. The elevated noise levels that begin to appear in the spectra after $t = 10$ s are attributed to these naturally forming air currents after the settling of the wake and the onset of rotor loads and loading noise. Further studies would need to be performed for these postulations to be confirmed.

Spectra from all microphones are plotted in Figs. 12a and 12b corresponding to the $\alpha = 0$ deg and $\alpha = 15$

deg blade pitch angle conditions, respectively. Subsequent spectra are shifted by 20 dB to reduce clutter. These spectra are computed using signals captured at the fourth radial measurement position at $r/D = 2.5$. The shapes of the spectra comprise all of the traditional hallmarks of the acoustic footprint generated by a hovering rotor. That is, there is a manifestation of harmonics linked to the fundamental blade pass frequency that eventually decay at higher frequencies. The valleys buried between these tones comprise signatures of rotor broadband noise with peaks occurring for all observers around $f = 10f_b$ for the $\alpha = 0$ deg, that increase to $f = 20f_b$ for the $\alpha = 15$ deg condition. Peaks not associated with the blade pass frequency harmonics are the consequence of motor noise and are more significant at the $\alpha = 0$ deg blade pitch condition.

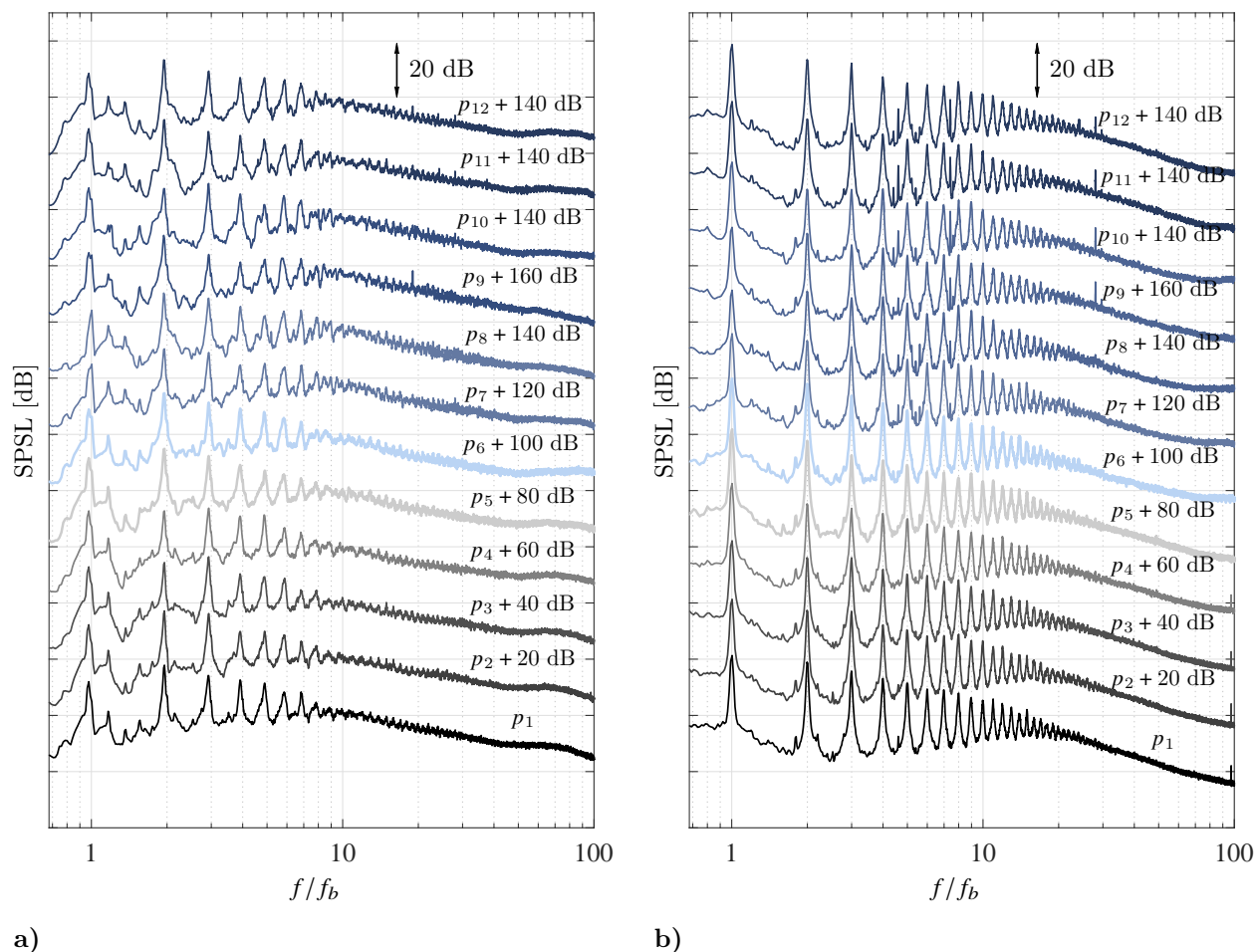


Figure 12: a) SPSL [dB] of all microphones at $r/D = 2.5$ for the 5-bladed rotor at $\omega = 30$ rps and a) $\alpha = 0$ deg, and b) $\alpha = 15$ deg blade pitch angles.

Moving to Figs. 13a and 13b, the effect of pitch angle on the pressure spectra are shown for observers located at the rotor disk plane ($\theta = 0$ deg) and below ($\theta = -38$ deg), respectively. One can see an immediate increase in the amplitude of the fundamental blade pass frequency with increasing blade pitch, as well as a shift in the rotor broadband noise hump to higher frequencies. The grossest changes to the rotor broadband noise hump from a peak around $f = 10f_b$ to one around $f = 20f_b$ occurs between $0\text{deg} \leq \alpha \leq 6\text{deg}$. As blade pitch angles increase further, the location of the rotor broadband noise hump remains fixed. This demonstrates how the source of rotor broadband noise remains unchanged at higher blade pitch angles when the inflow is capable of sufficiently pushing the rotor blade wake below the rotor disk plane.

Contours of the overall sound pressure level (OASPL, [dB]) are shown in Fig. 14 for all blade pitch angles of the 5-bladed rotor at $\omega = 30$ rps. The findings are referenced to the rotor hub at $(r, z)/D = (0, 0)$. The same contour lines and colors are used for all figures with step increments corresponding to a change of 2 dB. OASPL levels are obtained by integrating the noise spectra over the frequency range $0.9N_b\omega \geq f \geq f_N$

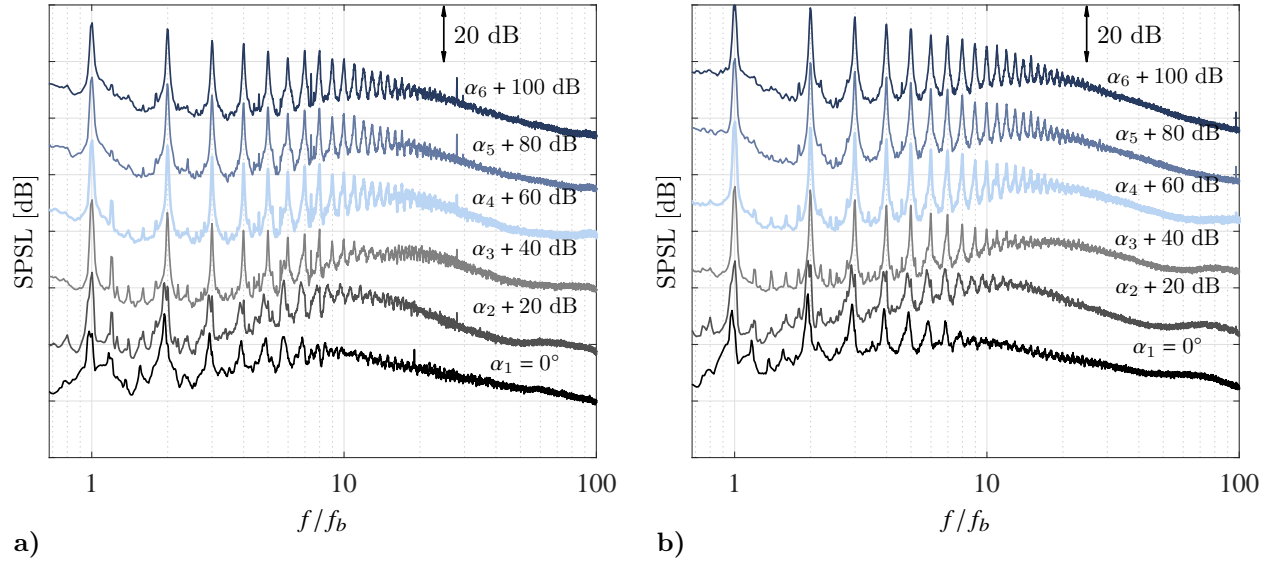


Figure 13: **Effect of blade pitch angle on SPSL [dB] for an observer located at $r/D = 2.5$ at the a) rotor disk plane, and b) below ($\theta = -38$ deg).** This is for the 5-bladed rotor at $\omega = 30$ rps.

where f_N is the nyquist frequency. This has the benefit of eliminating background noise from the calculation. A dipole-like directivity pattern centered on the rotor disk plane is revealed with similar size lobes appearing both above and below the rotor disk plane. These same shapes persist for all blade pitch angles and with comparable levels. Similar findings have been reported by others in the open literature.^{19–22} These lobes are the same for all blade pitch angles and are attributed to loading noise.²³ Thickness noise²⁴ is isolated to the first rotor harmonic and is present here as well (not shown).

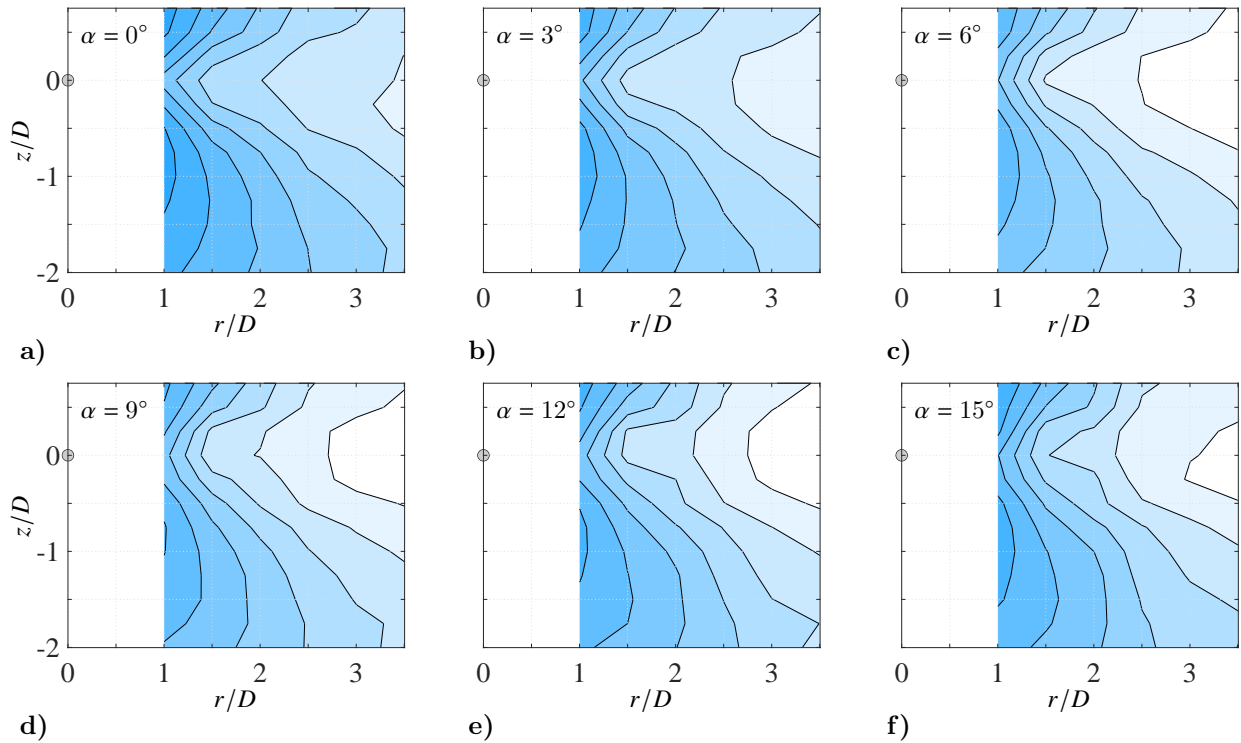


Figure 14: **OASPL [dB] contour across the full 2D measurement grid for different blade pitch angles of the 5-bladed rotor at $\omega = 30$ rps.** Contour step increments are 2 dB.

Given the close proximity of the microphone array to the rotor, pressure waveforms are scrutinized in order to identify two features important to measurements of this kind. The first is to determine the location where hydrodynamic effects no longer contribute to the pressure waveform following the same procedure described by Tinney and Sirohi.⁵ That is, close to the rotor, the pressure field is a manifestation of both hydrodynamic and acoustic waveforms with the hydrodynamic component being the dominant of the two, and with a roll-off that scales like $p \propto 1/r^3$; see Arndt et al.²⁵ for a derivation of this scaling law. Farther from the rotor, hydrodynamic effects disappear so that only the acoustic component remains. As such, pressure waveforms then decay spherically according to $p \propto 1/r$. Separating acoustic and hydrodynamic components of the pressure waveform is not trivial and requires information concerning the wavespeed of the various instability waves.

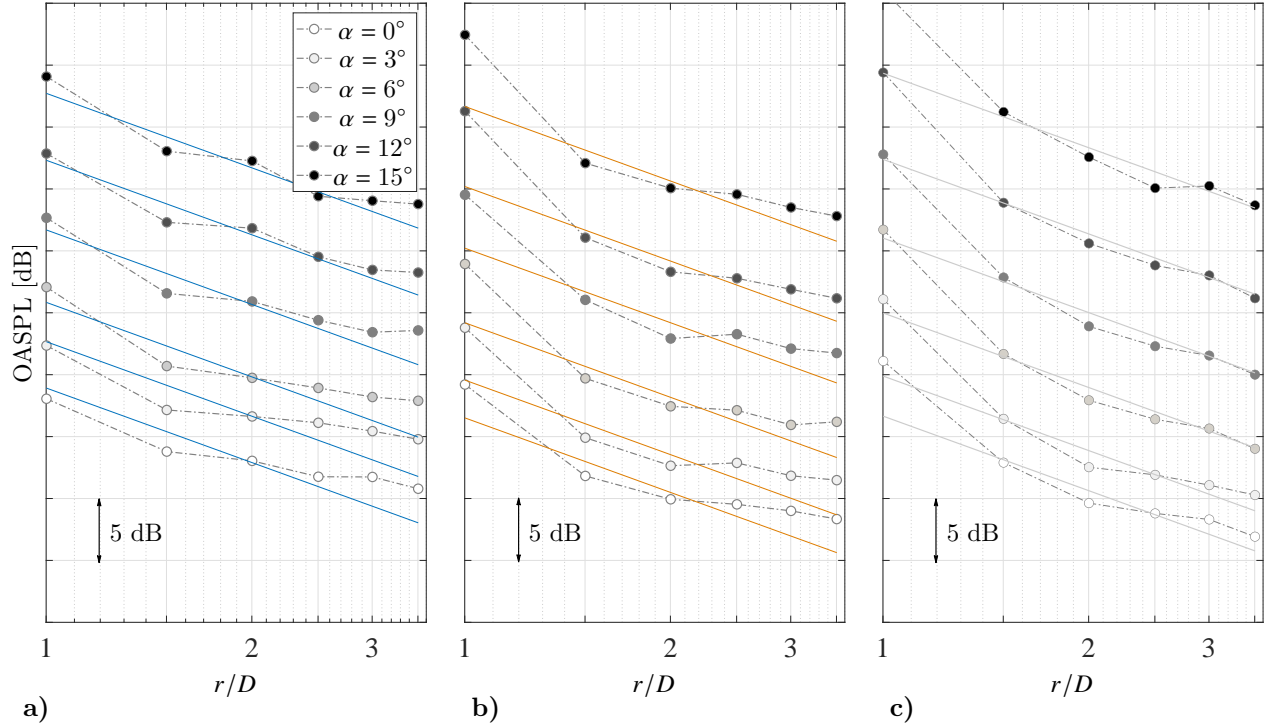


Figure 15: OASPL [dB] along the rotor disk plane for different blade pitch angles of the a) 5-bladed, b) 4-bladed, and c) 3-bladed rotor at $\omega = 30$ rps. Colored lines highlight spherical decay.

To see where the pressure field transitions from being dominated by hydrodynamic waveforms, to ones that are purely acoustic, pressure waveforms registered along the rotor disk plane are shown in Fig. 15 superposed the spherical decay trend. This is shown for the 5-bladed rotor in Fig. 15a, the 4-bladed rotor in Fig. 15b, and the 3-bladed rotor in Fig. 15c, for the same rotor speed ($\omega = 30$ rps) and all pitch angles ($\alpha = 0$ deg to 15 deg). Starting with the 5-bladed rotor, at low pitch angles, the spherical decay trend matches fairly well within the first two rotor diameters suggesting that the hydrodynamic to acoustic transition zone is close to the rotor for this kind of setup. This would require a finer measurement grid at positions close to the rotor. Likewise, small departures from the $1/r$ trend at farther positions and low pitch angles suggest that facility reflections are impacting the measurements for some of these conditions, or that the true source is not located at the rotor hub for observers located at the rotor disk plane. These same observations have been reported elsewhere using smaller scale rotors.²⁰ Where the 4-bladed rotor is concerned, the hydrodynamic to acoustic transition region appears between $1 \leq r/D \leq 1.5$, after which, pressure waveforms decay proportionately with increasing distance. Small departures from the $1/r$ trend are also observed after two rotor diameters from the hub and for low pitch angles, which lessen with increasing collective pitch settings. As for the 3-bladed rotor configuration, the transition between hydrodynamic and acoustic fields is similar to the 4-bladed rotor, but with a smoother acoustic decay beyond $r/D \geq 2.5$. The overall findings demonstrate that the acoustic field for this rotor begins after 1.5 rotor diameters from the hub while spherical decay, for the most part, is

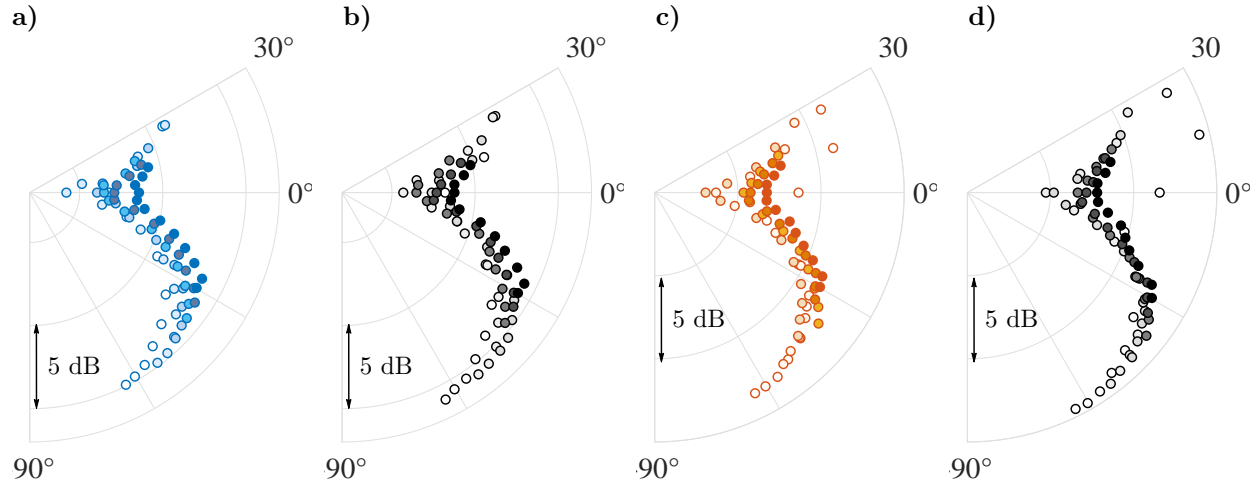


Figure 16: **OASPL [dB] of all microphones projected to a common distance for the 5-bladed rotor at a) $\alpha = 9$ deg, and b) $\alpha = 15$ deg, and the 4-bladed rotor at c) $\alpha = 9$ deg, and d) $\alpha = 15$ deg for $\omega = 30$ rps.**

being preserved at higher blade pitch angles.

For the other microphone observers located above and below the rotor disk plane, there is interest in seeing how well they abide by the spherical decay rule. Therefore, microphone measurements comprising the full 2D grid are projected to a common distance assuming $p \propto 1/r$. This is shown in Fig. 16 for only a subset of the full database. Figs. 16a and 16b are for the 5-bladed rotor at 30 rps and for pitch angles of $\alpha = 9$ deg, and $\alpha = 15$ deg, respectively. Open and closed symbols correspond to microphone array positions at $r/D = 1.0$ and $r/D = 3.5$, respectively. As expected, observers located closest to the rotor do not abide by spherical decay as they are hydrodynamic in nature. Farther away, the results collapse reasonably well under these conditions. The findings suggest that the pressure field along lines above and below the rotor disk plane are acoustic and collapse reasonably well using a source centered at the rotor hub. The same is true for the 4-bladed rotor as shown in Figs. 16c and 16d.

V. Acknowledgements

Support for this effort was graciously provided through an internal research and development award provided by the Signal and Information Sciences Laboratory of the Applied Research Laboratories, The University of Texas at Austin. Special thanks to Neal A. Pandey for his assistance with the design of the upper rotor assembly. The data presented in this study and will be made available for download at <https://www.arlut.utexas.edu/gdl/downloads>

References

- ¹Jia, Z., and Lee, S., “Computational study on noise of urban air mobility quadrotor aircraft,” *The Journal of the American Helicopter Society*, Vol. 67, No. 012009, 2022, pp. 1-15.
- ²Lee, S., Ayton, L., Bertagnolio, F., Moreau, S., Chong, T. P., and Joseph, P., “Turbulent boundary layer trailing-edge noise: Theory, computation, experiment, and application,” *Progress in Aerospace Sciences*, Vol. 126, No. 100737, 2021.
- ³Faraaz, M., Faizan, A., Badarinath, M., Subramaniyan, K. V., Harursampath, D., and Gupta, R. B., “Baseline design of propeller for an eVTOL aircraft to achieve urban air mobility,” *2023 IEEE Aerospace Conference*, Big Sky, MT, USA, 2023, pp. 1-10, doi: 10.1109/AERO55745.2023.10115797.
- ⁴Stoll, A., and Bevirt, J.B., “Development of eVTOL Aircraft for Urban Air Mobility at Joby Aviation,” *Vertical Flight Society 78th Annual Forum*, 2022.
- ⁵Tinney, C.E. and Sirohi, J., “Multicopter Drone Noise at Static Thrust,” *AIAA Journal*, Vol. 56, No. 7, 2018.
- ⁶Tinney, C. E., and Valdez, J., “Acoustic Scaling for Rotors in Hover,” *American Helicopter Society 75th Annual Forum*, 2019.
- ⁷Tinney, C.E., and Valdez, J.A., “Thrust and Acoustic Performance of Small-Scale, Coaxial, Co-rotating Rotors in Hover,” *AIAA Journal*, Vol. 58, No. 4, 2020.
- ⁸Conlisk, A. T., “Modern Helicopter Aerodynamics”, *Annu. Rev. Fluid Mech.*, Vol. 29, 1997, pp. 515-567.

- ⁹Leishman, G.J., "Principles of Helicopter Aerodynamics," *Cambridge University Press*, Cambridge, 2006.
- ¹⁰Fradenburgh, E. A., "The helicopter and the Ground Effect Machine," *Journal of the American Helicopter Society*, Vol. 5, 1960, pp. 24-33.
- ¹¹Tanner, P. E., Overmeyer, A.D., Jenkins, L. N., Yao, C., and Bartram, S. C., "Experimental Investigation of Rotorcraft Outwash in Ground Effect," *American Helicopter Society 71st Forum*, 2015.
- ¹²Pasquali, C., Poggi, C., Bernardini, G., Serafini, J., and Gennaretti, M., "Aeroacoustic analysis of helicopter rotors in ground effect," *25th AIAA/CEAS Aeroacoustics Conference*, 2019.
- ¹³McCoy, M., and Wadcock, A. J., "Documentation of the recirculation in a closed-chamber rotor hover test," *NASA Technical Memorandum*, NASA-TM-2016-219162, 2016.
- ¹⁴Schiller, N. H., Pascioni, K. A., and Zawodny, N. S., "Tonal Noise Control using Rotor Phase Synchronization," *American Helicopter Society 75th Annual Forum*, 2019.
- ¹⁵Pandey, N., Valdez, J. A., Beaman, W., and Tinney, C. E., "Acoustics of Side-by-Side Synchrophased Rotors," *AIAA/CEAS Aeroacoustics Conference*, Rome, Italy, 2024, AIAA Paper 2024-3234.
- ¹⁶Rayes, S., "How to Match a Measurement Microphone to a Sound Field," *G.R.A.S. Sound and Vibration Handbook*, 2021, pp. 12.
- ¹⁷Weitsman, D., Stephenson, J. H., and Zawodny, N. S., "Effects of flow recirculation on acoustic and dynamic measurements of rotary-wing systems operating in closed anechoic chambers," *The Journal of the Acoustical Society of America*, vol. 148, No. 3, 2020, pp. 1325-1336.
- ¹⁸Amiet, R. K., "Noise produced by turbulent flow into a propeller of helicopter rotor," *AIAA Journal*, Vol. 15, No. 3, 1977, pp. 307-308.
- ¹⁹Whiteside, S. K., Zawodny, N. S., Fei, X., Pettingill, N., Patterson, M. D., and Rothhaar, P. M., "An exploration of the performance and acoustic characteristics of UAV-scale stacked rotor configurations," *AIAA SciTech Forum*, San Diego, 2019, AIAA Paper 2019-1071.
- ²⁰Baars, W. J., Grande, E., and Ragni, D., "Noise metrics of the time varying acoustic far-field of rotors," *NOISE-CON*, June 2022, Lexington, KY, Vol. 12, pp. 270-281.
- ²¹Grande, E., Romani, G., Ragni, D., Avallone, F., and Casalino, D., "Aeroacoustic Investigation of a Propeller Operating at Low Reynolds Numbers," *AIAA Journal*, Vol. 60, No. 2, 2022, pp. 860-871, DOI: 10.2514/1.J060611.
- ²²Baars, W. J., and Ragni, D., "Low-frequency Intensity Modulation of High-Frequency Rotor Noise," *AIAA Aviation Forum*, San Diego, 2023, AIAA Paper 2023-3215.
- ²³Brentner K.S., and Farassat, F., "Modeling Aerodynamically Generated Sound of Helicopter Rotors," *Progress in Aerospace Sciences*, Vol. 39, No. 2-3, February - April 2003, pp. 83-120.
- ²⁴Dahan, C., and Gratioux, E., "Helicopter Rotor Thickness Noise," *J. Aircraft*, Vol. 18, No. 6, 1981, pp. 487-494.
- ²⁵Arndt, R. E. A., Long, D. F., and Glasuer, M. N., "The proper orthogonal decomposition of pressure fluctuations surrounding a turbulent jet," *J. Fluid Mech.*, Vol. 340, 1997, pp. 1-33.